



Final Draft of the original manuscript

Kainz, C.; Schalk, N.; Tkadletz, M.; Saringer, C.; Winkler, M.; Stark, A.; Schell, N.; Julin, J.; Czettl, C.:

Thermo-physical properties of coatings in the Ti(B,N) system grown by chemical vapor deposition.

In: Surface and Coatings Technology. Vol. 384 (2020) 125318.

First published online by Elsevier: 28.12.2019

<https://dx.doi.org/10.1016/j.surfcoat.2019.125318>

Thermo-physical properties of coatings in the Ti(B,N) system grown by chemical vapor deposition

Christina Kainz¹, Nina Schalk¹, Michael Tkadletz², Christian Saringer¹, Markus Winkler³,
Andreas Stark⁴, Norbert Schell⁴, Jaakko Julin⁵, Christoph Czettel⁶

¹ *Christian Doppler Laboratory for Advanced Coated Cutting Tools at the Department of Materials Science, Montanuniversität Leoben, Franz-Josef-Straße 18, 8700 Leoben, Austria*

² *Department of Materials Science, Montanuniversität Leoben, Franz-Josef-Straße 18, 8700 Leoben, Austria*

³ *Department Thermal Energy Converters, Fraunhofer Institute for Physical Measurement Techniques IPM, Heidenhofstraße 8, 79110 Freiburg, Germany*

⁴ *Institute of Materials Research, Helmholtz-Zentrum Geesthacht, Max-Planck-Straße 1, 21502 Geesthacht, Germany*

⁵ *Institute of Ion Beam Physics and Materials Research, Helmholtz-Zentrum Dresden-Rossendorf, Bautzner Landstraße 400, 01328 Dresden, Germany*

⁶ *Ceratizit Austria GmbH, Metallwerk-Plansee-Straße 71, 6600 Reutte, Austria*

Keywords: Chemical vapor deposition, X-ray diffraction, Ti(B,N), thermal conductivity, strain

Abstract

Hard protective coatings are commonly subjected to temperatures exceeding 1000 °C, which has significant influence on their thermo-physical properties and the associated performance in application. Within the present work, temperature dependent physical properties of coatings within the Ti(B,N) system grown by chemical vapor deposition were correlated with their chemical composition. High-energy X-ray diffraction experiments in inert atmosphere proved that TiN, TiB₂ and ternary TiB_xN_y coatings with varying B contents are thermally stable up to 1000 °C. In-plane

strains of TiN and TiB_xN_y coatings diminish during heating, whereas TiB_2 exhibits compressive strain enhancement up to the deposition temperature. Nanocrystalline TiB_2 exhibits more pronounced grain growth during annealing compared to coarse grained columnar TiN. Within the investigated coatings, the mean thermal expansion coefficient decreases as the B content increases. The same trend was observed for the thermal conductivity, which correlates with the grain size of the coatings.

1. Introduction

Ternary TiB_xN_y coatings are commonly used for the protection of tools during metal cutting, as they are reported to show high hardness, combined with excellent wear resistance and oxidation stability [1,2]. The outstanding properties of TiB_xN_y coatings are mainly attributed to their nanocrystallinity and nanocomposite structure consisting of face centered cubic (fcc) TiN and hexagonal (h) TiB_2 . A vast number of publications is dedicated to TiB_xN_y coatings with different B contents prepared by physical vapor deposition [3–6]. However, it is also possible to deposit TiB_xN_y using chemical vapor deposition (CVD), where the B content is adjusted by the relative amount of the B precursor in the feed gas. Microstructure, mechanical properties, tribological behavior as well as cutting performance of CVD Ti(B,N) have been investigated in the past [7,8]. The hardness of coatings within the Ti(B,N) system is reported to increase with B addition, with the hardest being TiB_2 . However, a significant hardness drop was observed by Tkadletz *et al.* at a B content of ~45 at.%. This deterioration of the hardness was correlated with the transition from a fcc-TiN dominating structure to sub-stoichiometric h- $TiB_{2-x}N_y$ [7,9]. In CVD TiB_xN_y coatings with B contents <18 at.%, amorphous TiB was observed by Dreiling *et al.*, who reported that this compound improves the oxidation resistance within the Ti(B,N) system [10].

As protective coatings for cutting applications are subjected to temperatures, which may exceed 1000 °C, their thermal stability is of major importance [11]. In order to prevent the

underlying tool from overheating, the coating should additionally exhibit good heat barrier properties. Ideally, the film should possess a low thermal conductivity out-of-plane to protect the substrate from overheating and a high one in-plane to dissipate the heat from the contact zone [12]. A further aspect that has to be considered is the mismatch in thermal expansion coefficient of coating and substrate, which should favorably be low. Otherwise cracks may arise during cooling or application, which fosters oxidation and wear [13]. However, detailed information on the thermo-physical properties of CVD coatings in the Ti(B,N) system is missing in literature.

Thus, the goal of this work is to provide a summary on the thermo-physical properties of CVD coatings ranging from pure TiN over ternary TiB_xN_y coatings with different composition to pure TiB_2 . High energy X-ray diffraction (HE-XRD) at a synchrotron radiation source was used to monitor the phase stability, thermal expansion and lattice strain of the different phases in the coatings as a function of the temperature. Additionally, the thermal conductivity of the coatings was evaluated as a function of B content in order to assess their potential use as heat barriers.

2. Experimental methods

Coating depositions were carried out in a SuCoTec SCT600 TH industrial-scale thermal CVD plant using a gas mixture comprising $TiCl_4$, H_2 , N_2 and Ar to synthesize TiN. BCl_3 was supplied additionally in the depositions of the B containing coatings and N_2 was omitted to obtain pure TiB_2 . Further details on the deposition conditions can be found in ref. [14]. The resulting coating thickness ranged from 4.0 to 7.1 μm and the growth rate was between 0.76 and 1.64 $\mu m/h$. Cemented carbide cutting inserts with 92 wt.% WC, 6 wt.% Co and 2 wt.% mixed carbides in SNUN geometry (ISO 1832) served as substrate. In order to prevent B diffusion into the substrate, a $\sim 0.2 \mu m$ thick TiN base-layer was applied underneath the B containing coatings. TiN and TiB_2

were additionally deposited onto Fe foil. In order to obtain TiN and TiB₂ powders, the Fe substrates were then dissolved in an aqueous solution of HNO₃ (20 vol. %) at 70 °C for 1 h.

The chemical composition of the B containing coatings was determined by means of elastic recoil detection analysis (ERDA) using a 43 MeV³⁵Cl⁷⁺ ion beam and a Bragg ionization chamber in 30 ° angle with respect to the beam. Energy dispersive X-ray spectroscopy (EDX) was used in order to determine the elemental composition of TiN [15]. The EDX measurement was carried out with an Oxford Instruments INCA spectrometer, equipped with an INCA extension mounted on a Zeiss EVO50 scanning electron microscope (SEM).

For a first assessment of the microstructure of the as-deposited and annealed Ti(B,N) coatings, a Bruker AXS D8 Advance diffractometer in grazing incidence geometry (incidence angle 2°) with Cu-K_α radiation was used. TiN and TiB₂ coatings were annealed in an HTM Reetz vacuum furnace at a base pressure of 5×10⁻⁶ mbar and 1000 °C for 15 and 120 minutes. The morphology of as-deposited and annealed TiN and TiB₂ coatings was compared using a field emission gun SEM of type Zeiss Auriga.

HE-XRD investigations were carried out at the P07 High Energy Materials Science Beamline of the Helmholtz Zentrum Geesthacht at DESY. For that purpose, samples with a size of 4×4×8 mm³ were prepared by mechanical cutting. The experiments were conducted using a monochromatic synchrotron beam with an energy of 87.1 keV and a cross-section of 400×100 μm². Figure 1 shows a schematic view of the test set-up used for the determination of the temperature dependent phase evolution, lattice expansion and strain of the coatings. The chosen maximum temperature for all six samples was 1000 °C, as this is a realistic temperature arising during metal cutting. A coil heated the substrate inductively and the temperature was monitored with a thermocouple mounted to the substrate material. In order to prevent oxidation, heating was performed in Ar atmosphere. Debye-Scherrer rings were collected in transmission geometry on a

Perkin Elmer XRD 1621 flat panel detector. The geometric relations between sample and detector were calibrated with a LaB₆ powder standard. The one dimensional data obtained through azimuthal integration over the entire angular range were used to compile temperature resolved phase plots of the coatings. Evaluation of the 2D diffraction data was conducted using the software DAWN 2 [16]. In addition to phase identification, the distortion of the obtained Debye-Scherrer rings allowed the determination of the temperature dependent in-plane strain. The Debye-Scherrer rings of the (200) reflection in case of the TiN and (101) in case of the TiB₂ phase were divided into cake segments of 10° and azimuthally integrated. Due to the low intensity of the reflections in the lower part of the Debye-Scherrer rings, resulting from the absorption of the cemented carbide substrate (compare Figure 1), only the upper part was used for the evaluation. The peak positions were fitted applying a Pseudo-Voigt function. A custom made Python script allowed processing of the data following the sin²ψ-method to obtain the lattice strain.

Analysis of the thermal expansion of the coatings in the temperature range 25-860 °C was performed according to the method reported by James *et al.* [17]. 860°C was chosen as the maximum temperature for this evaluation, as this was the lowest applied deposition temperature. The (200) reflection was used in case of fcc-TiN and the (101) reflection in case of h-TiB₂. h-TiB₂ exhibits a different thermal expansion in a and c direction [18]. Eq. (1) enables to calculate an averaged mean thermal expansion coefficient $\alpha_{a,c}$ by

$$\alpha_{a,c} = \frac{2\alpha_a + \alpha_c}{3} \quad [18]. \quad (1)$$

For the ternary TiB_xN_y coatings, the expansion of both phases, fcc-TiN and h-TiB₂, was evaluated and averaged as a function of the actual B content to obtain α_m . The evaluation was conducted at the strain-free azimuthal angles calculated by

$$\cos\delta_0 \cos\theta_0 = \sqrt{\frac{1-\nu}{1+\nu}}, \quad (2)$$

with ν representing the Poisson's ratio of the respective material, δ_0 the strain-free azimuthal angle and θ_0 the conducted Bragg angle [19,20]. A segment of $\pm 5^\circ$ from the respective strain-free azimuthal angle was evaluated in order to obtain a reasonable data volume for the subsequent fit. Poisson's ratios of 0.23 and 0.11 were used for the calculation of the fcc-TiN and h-TiB₂ phases, respectively [18,21]. The obtained data were validated by comparison with the thermal expansion determined for powdered TiN and TiB₂ of the corresponding deposition runs. Therefore, diffractograms of these powders were recorded at the high-resolution powder diffraction beamline ID22 at the European Synchrotron Radiation Facility. The powders were encapsulated within a quartz capillary in Ar atmosphere and heated to 1000 °C. Pt powder served as standard for the temperature calibration. Detailed information on the measurement set-up for the powdered samples are given in ref. [22]. The lattice parameters of both, the powdered and solid coatings, were fitted applying a polynomial of second order to obtain α_{av} . In case of the solid coatings, α_{av} was determined from an average of the data gained at the two respective strain-free angles.

The thermal conductivity of the coatings in as-deposited state was determined by time-domain thermoreflectance (TDTR). For TiN and TiB₂, the annealed samples were also measured. TDTR measurements were conducted in out-of-plane direction and realized by a pulsed laser pump-probe system, as described in ref. [23]. The necessary laser pulses were generated by the Ti:Sapphire laser system Mai Tai from Spectra-Physics with a pulse width of 500 fs, a pulse repetition rate of 80 MHz, a wavelength of 785 nm and an average laser power (i.e. added average power of probe and pump beam) of 30 mW. The pump beam was modulated with a frequency of 11.1 MHz, resulting in an information depth between 0.25 and 0.64 μm [23]. The time delay between pump and probe beam was in the range of 0 to 3600 picoseconds. As a transducer layer, 70 nm of pure Al were deposited on the samples prior to the measurement. Directly before the

measurements on the samples, the measurement system was validated with two reference samples, namely a pure Si wafer and an oxidized one.

3. Results and discussion

The chemical composition of the coatings as determined by ERDA is shown in Figure 2a. For the nomenclature, the B and N content in the coatings was normalized to the Ti content. All coatings are located on the quasi-binary tie line of TiN-TiB₂, except TiB_{1.2}N_{0.56}, which is slightly shifted beside this line [24]. XRD investigations (Figure 2b) allowed the assessment of the microstructure of the coatings at room temperature (RT). With increasing amount of B in the coating, both, the intensity of the h-TiB₂ (101) reflection and the peak broadening gradually become more pronounced. The higher TiB₂ fraction explains the decrement in the Ti content with increasing B in the coating, as less Ti is needed for the formation of TiB₂ in comparison to TiN. The grain refinement is reflected in the evolution of the full width at half maxima (FWHM) shown in Figure 2c. An increment of the FWHM correlates with the smaller size of coherently diffracting domains [25]. In case of TiB₂, the (101) reflection was applied for the evaluation of the FWHM, whereas for the TiN and TiB_xN_y coatings the (200) reflection of fcc-TiN was used. The pronounced peak broadening of TiB_{1.2}N_{0.56} had already been observed by other authors and is suggested to result from the distorted structure and the concomitant high micro-strains of this coating [9]. From the lab scale X-ray diffractograms it may be assumed that only one peak is present at $2\theta \sim 42^\circ$, which seems to shift towards larger diffraction angles with increasing B content. However, the observed peak is comprised of the (101) h-peak of TiB₂ and the (200) fcc-peak of TiN as can be seen from the results of the HE-XRD in Figure 3. Thus, for the evaluation of the FWHM of the TiB_xN_y coatings, the peak was deconvoluted into two peaks, which were fitted using the Pseudo-Voigt function.

The temperature dependent phase plots in Figure 3 show a d-spacing range including the (200) fcc-TiN and (101) h-TiB₂ reflections. Standard d-spacings of these two phases at RT were taken from ICDD file # 00-038-1420 and # 01-071-0298 for fcc-TiN and h-TiB₂, respectively [26,27]. In agreement with the X-ray diffractograms given in Figure 2, the phase plot of the TiN coating shows only fcc-TiN [26]. With increasing amount of B, a second phase with a d-spacing of 2.06 Å emerges, which is assigned to h-TiB₂. Other minor intensities stem from the Co binder in the substrate. The (200) peak of fcc-TiN and the (101) peak of h-TiB₂ overlap in the lab-scale XRD (Figure 2b), however, differentiation of these two reflections is possible by means of HE-XRD. Up to TiB_{0.68}N_{0.64}, the signal of fcc-TiN is more pronounced than the one of h-TiB₂, which changes in case of TiB_{1.2}N_{0.56} in favor of h-TiB₂. None of the diffractograms show formation of additional phases at elevated temperatures. Temperature induced reactions between coating and substrate, as for instance the formation of brittle W-Co-B phases, can thus be excluded up to 1000 °C in protective atmosphere [28]. The ratio between fcc-TiN and h-TiB₂ in the ternary TiB_xN_y coatings seems to be, to a large extent, independent of the temperature. The position of the (200) peak of TiN is in reasonable good agreement with the one reported for fcc-TiN [26]. However, a slight peak shift is observable in case of the (101) reflection of h-TiB₂, which is more pronounced at lower B contents. This observation suggests the formation of a sub-stoichiometric h-TiB_{2-x}N_y structure, which converges to stoichiometric h-TiB₂ with increasing B content¹. At higher B contents there is less N incorporated in this h-phase, which is why the lattice expands less and thus the lattice parameter is smaller.

¹ For simplicity throughout the manuscript, the sub-stoichiometric h-TiB_{2-x}N_y phase in the ternary TiB_xN_y coatings will be denoted as h-TiB₂.

The temperature resolved HE-X-ray diffractograms allow the determination of the thermal expansion of the coatings. Figure 4 shows the mean coefficient of thermal expansion α_m in the temperature range 25-860 °C of the investigated coatings. Additionally, the estimated phase fraction of h-TiB₂ used for the calculation of α_m is plotted. This fraction was calculated according to the B content in the coating available for the formation of h-TiB₂, neglecting a possible sub-stoichiometric composition for this estimation. Further, it was assumed that no B is incorporated into the fcc-TiN lattice, which is in agreement with Nowotny *et al.* [24]. As can be seen in Figure 3, the h-TiB₂ phase shows a deviation from non-linear behavior when the deposition temperature (T_{dep}) is exceeded. In order to ensure that no effects other than the expansion of the lattice falsify the evaluation, the lowest applied T_{dep} was chosen as maximum temperature. The mean thermal expansion coefficient of the investigated coatings gradually decreases as a function of increasing B content. Thus, a lower mismatch of α_m between coating and the used cemented carbide substrate ($5.5 \times 10^{-6} \text{ K}^{-1}$) is achieved when applying protective coatings with high B contents [29]. Consequently, B rich coatings should be chosen in favor over TiN and B lean coatings in regard of the thermal expansion coefficient to possibly retard crack formation [13]. However, it should be noted that the deposition of B containing coatings onto cemented carbide always requires a base-layer in order to prevent B diffusion into the substrate. Otherwise, the resulting formation of brittle W-Co-B phases causes decarburization of the substrate, which deteriorates the cutting performance [28]. Thus, commonly a TiN base layer is applied underneath TiB₂. The adhesion problem between these two layers, which arises from the difference in crystal structure, stresses and grain size, can be overcome by using an additional graded TiB_xN_y transition layer. The ternary TiB_xN_y coatings investigated within this study were shown to be suitable for cutting applications as a graded interlayer stack between binary TiN and TiB₂ [9,14].

Commonly, the thermal expansion coefficient is determined by XRD using powdered samples [30,31]. Thus, the herein obtained values for α_{av} for solid coatings were validated through comparison with powders of TiN and TiB₂ coatings of the respective deposition runs. An excellent agreement between the TiN powder ($8.94 \times 10^{-6} \text{ K}^{-1}$) and the solid coating ($8.94 \times 10^{-6} \text{ K}^{-1}$) was found using the Poisson's ratio reported by Almer *et al.* [21]. This was also true in case of TiB₂, when using the Poisson's ratio reported by Munro [18]. The powder exhibited a value of $\alpha_m = 7.40 \times 10^{-6} \text{ K}^{-1}$ and the solid coating $\alpha_m = 7.56 \times 10^{-6} \text{ K}^{-1}$, verifying the feasibility of determining the thermal expansion coefficient on intact coatings.

The temperature dependent evolution of the in-plane strains of the investigated coatings is shown in Figure 5. It should be pointed out that the calculation of the strain is based solely on one orientation for each phase, being (200) in fcc-TiN and (101) in h-TiB₂. In case of TiB_{0.12}N_{0.93} and TiB_{0.31}N_{0.84}, only the strain in the fcc-phase could be evaluated, due to the minor fractions and thus low signal intensity of h-TiB₂ within these coatings. In the ternary coatings with higher fractions of the h-TiB₂ phase, both the strain within the fcc- and the h-phase was investigated. Nevertheless, a reasonable evaluation could be achieved. The results in Figure 5 demonstrate how different phases influence each other during thermal treatment. At RT, the strain in the fcc-phase within TiN and the ternary coatings (Figure 5a) is tensile due to the higher thermal expansion coefficient of the coating in comparison to the substrate. With increasing fraction of h-TiB₂ in the coating, the tensile strain in the fcc-TiN phase at RT increases to its highest value in TiB_{1.2}N_{0.56}. It is assumed that the reason for that are coherency strains, which arise as a result of the coherent epitaxial relationship between fcc-TiN and h-TiB₂ [32]. The strain of the fcc-phase within TiN and the ternary coatings changes from tensile at RT to unstrained or slightly compressive at the respective T_{dep}. This change becomes more pronounced with increasing fraction of the h-TiB₂ phase, as evidenced in Figure 5b and c. Regarding the h-phase, a higher fraction of fcc-TiN in the coating is

suggested to provoke both, higher compressive strains at RT and stronger change of the strain during heating (Figure 5b and c). With increasing temperature, the strain of the h-phase in the ternary coatings moves towards a tensile strained state, which is in contrast to binary TiB₂, where the strain becomes more compressive up to T_{dep}. Afterwards, the coating strain of TiB₂ shows a pronounced relaxation up to the maximum test temperature of 1000 °C. This behavior was not observed for the h-phase in the ternary coatings. It may thus be suggested that the presence of the second phase impedes the relaxation. The reason for the compressive strains in CVD TiB₂ coatings is up to now not entirely understood. However, the higher Laplace pressure due to the high surface energy and nanocrystalline grain size of TiB₂ was suggested by Schalk *et al.* as a possible source for the compressive strains [33,34]. During cooling, the tensile strain of the fcc-phase increases again for TiN and the ternary coatings. TiN shows a deviation from the linear strain evolution in the cooling curve. The most plausible reason for this is formation of thermal cracks, as was reported by Bartosik *et al.* for CVD TiN coatings [35]. The presence of such cracks in the here investigated TiN was verified by SEM, as is shown below in Figure 7. While a slight kink may also be suggested from the cooling curve of TiB_{0.12}N_{0.93}, the tensile strain of the fcc-phase within the other coatings do not display this feature. Otherwise, the TiB_xN_y coatings show only minor deviations of the strain during heating and cooling, which is true both for the fcc- and the h-phase. Therefore, the extent of relaxation of strains during heating is low. Contrarily, a major difference between the heating and cooling curve in pure TiB₂ is evident. The strain within this coating does not change noteworthy during cooling and the coating remains in a slightly tensile strained state. A further decisive aspect that has to be considered in the discussion of the strains is the texture of the coatings. The intensity of the peaks was largely invariant on the azimuth in case of the binary coatings and the (220) fcc-TiN reflection of the ternary ones. This was not the case for the (101) h-TiB₂

reflection in the TiB_xN_y coatings, which indicates the presence of a texture. However, the $\sin^2\psi$ plots were linear and thus the effect of the texture on the strains is suggested to be negligible.

Being a measure of the distribution of heat within a tool, the thermal conductivity is a decisive parameter when evaluating the suitability of a material for a given application [30]. Figure 6 shows the estimated specific heat capacity c_p and the measured thermal conductivity λ of the investigated coatings. c_p of the TiB_xN_y coatings was averaged from the values of TiN and TiB_2 in dependence of the estimated fraction of the h- TiB_2 phase applying the rule of mixture [18,36]. Provided that the TiB_2 content in the sample is directly related to the B content, the specific heat capacity decreases when going from B poor to B rich samples. The thermal conductivity decreases inversely proportional with the B content. While the highest value was found for TiN (45 W/mK), $\text{TiB}_{1.2}\text{N}_{0.56}$ features the lowermost one with 7 W/mK. This behavior can be ascribed to the grain refinement through B addition. With decreasing grain size and concomitant higher defect density, the phonon scattering increases and consequentially the thermal conductivity declines. The fact that TiB_2 exhibits a higher thermal conductivity (14 W/mK) in comparison to $\text{TiB}_{1.2}\text{N}_{0.56}$ is assigned to the alloy scattering in the ternary coatings. The thermal conductivity of TiB_2 in the present study is low in comparison to data reported in literature (96 W/mK). This discrepancy is most likely due to the difference in microstructure between the nanocrystalline TiB_2 in our study and the material in the reference with a grain size of 12 μm [18]. A similar situation applies to TiN. The columnar grains of TiN in our study partly extend over the whole coating thickness of $\sim 6 \mu\text{m}$. In comparison, Samani *et al.* report a thermal conductivity of 11 W/mK in a TiN coating with a thickness of 1.2 μm and thus smaller grain size in growth direction [37]. The larger grain size and thus less pronounced phonon scattering of TiN in our work explains the discrepancy. As the h- TiB_2 phase in $\text{TiB}_{0.68}\text{N}_{0.64}$ and $\text{TiB}_{1.2}\text{N}_{0.56}$ exhibited a texture, a possible anisotropy of the thermal conductivity cannot be fully excluded. However, as the TiB_2 is reported to be nanocrystalline and

distributed between the larger TiN grains, the effect is assumed to be negligible [33,38]. It should be emphasized at this point that the thermal conductivity was determined in out-of-plane direction, while the strains and thermal expansion refer to the in-plane direction. Furthermore, the information depth was noteworthy lower in the TDTR measurements (0.25 and 0.64 μm) in comparison to the synchrotron experiments, where the whole coating thickness was probed. Thus, possible gradients in stress, grain size and texture over the coating thickness may affect the results of the two measurements in a different extent. The impact of annealing on the coatings' microstructure is reflected in the thermal conductivity. There is no major change of this parameter when annealing TiN for 15 or 120 minutes at 1000 °C. Contrarily, the annealing of TiB₂ results in an increase from 14 W/mK in the as-deposited state to 26 W/mK and 37 W/mK in the coating annealed for 15 and 120 minutes, respectively. These observations suggest that TiB₂ undergoes more pronounced grain growth and defect annihilation during annealing at 1000 °C compared to TiN.

The cross-section morphologies of TiN and TiB₂ in as-deposited and annealed state (Figure 7) verify this presumption. While no major difference between the micrographs of as-deposited and annealed TiN is visible, grain growth is unambiguously observable in the heat treated TiB₂ coatings. After 15 minutes of annealing, only a few larger grains are visible, however, grain growth becomes clearly evident after heat treatment for 120 minutes. The behavior of the FWHM follows the same trend: the peak broadening of TiN, determined on the (200) reflection, was invariant on the heat treatment. Contrarily, the FWHM of the (101) reflection of TiB₂ decreases from 1.00° in the as-deposited state to 0.73° and 0.35° after annealing for 15 and 120 minutes, respectively. Considering both, the cross-section morphology and FWHM, it may be concluded that the reduced FWHM in the TiB₂ coating annealed for 15 minutes is mainly related to defect annihilation. The reason for the pronounced grain growth in TiB₂ is due to its high number of grain

boundaries. As they constitute defects in a perfect lattice, reduction of the grain boundary area results in a decrement of the Gibbs free energy [39]. The cross-sectional crack depicted in the micrograph of as-deposited TiN (Figure 7a) is representative for the morphology of this coating. These cracks arise in TiN during cooling after the deposition, as was discussed above (compare also Figure 5a). Cracks were not observable in case of TiB₂, which is suggested to stem from the nanocrystalline grains and concomitant high strength according to the Hall-Petch effect [40,41]. Furthermore, the higher K_{IC} value of TiB₂ (6.2 MPa/m^{1/2}) in comparison to TiN (1.2 – 3 MPa/m^{1/2}) and thus better resistance to crack propagation explains the lower abundance of cracks in TiB₂ [18,42,43].

In order to summarize the findings gathered within this work, Table 1 gives the numerical values of the coating thickness, thermal expansion coefficient, specific heat capacity and thermal conductivity of the investigated coatings as a reference.

Table 1: Summary of thermo-physical properties of all investigated Ti(B,N) coatings

	Coating thickness [μm]	¹ $\alpha_m \times 10^{-6}$ [K^{-1}]	² λ [W/mK]	³ $c_p \times 10^6$ [$\text{J/m}^3\text{K}$]
TiN	7.1	8.94	45	3.14
TiB_{0.12}N_{0.93}	5.0	8.93	35	3.12
TiB_{0.31}N_{0.84}	5.4	8.70	26	3.09
TiB_{0.68}N_{0.64}	5.9	8.51	23	3.02
TiB_{1.2}N_{0.56}	7.4	8.50	7	2.94
TiB₂	4.1	7.57	14	2.84

¹ mean coefficient of thermal expansion (25-860 °C), ² thermal conductivity, ³ specific heat capacity

4. Conclusions

TiN, TiB₂ and TiB_xN_y coatings with varying B contents have been grown by thermally activated chemical vapor deposition and their thermo-physical properties have been studied.

HE-XRD experiments showed that annealing the coatings in protective atmosphere between 25 and 1000 °C does not alter the phase composition. The thermal expansion, directly determined from the coatings on the substrate, declines as the B content increases. TiB₂ exhibits an increment of the in-plane compressive lattice strain during heating up to T_{dep}. The relaxation of the in-plane tensile strains during cooling in TiN is suggested to result from the formation of thermal cracks. In the ternary coatings, both the tensile strains in the fcc- and the compressive strains in the h-phase diminish as the thermal load increases to the deposition temperature. The thermal conductivity in the coatings decreases with increasing B content, which is ascribed to increased phonon scattering as a result of smaller grain size and higher defect density. The results gained within this work give an overview of selected thermo-physical properties of CVD coatings in Ti(B,N) system and thus allow for a better understanding of these application relevant materials.

Acknowledgements

The authors thank Bernhard Sartory (Materials Center Leoben) for FIB-SEM work. The financial support by the Austrian Federal Ministry for Digital and Economic Affairs and the National Foundation for Research, Technology and Development is gratefully acknowledged. The authors gratefully acknowledge the financial support under the scope of the COMET program within the K2 Center “Integrated Computational Material, Process and Product Engineering (IC-MPPE)” (Project No 859480). This program is supported by the Austrian Federal Ministries for Transport, Innovation and Technology (BMVIT) and for Digital and Economic Affairs (BMDW), represented by the Austrian research funding association (FFG), and the federal states of Styria, Upper Austria and Tyrol.

References

- [1] P.H. Mayrhofer, C. Mitterer, High-temperature properties of nanocomposite TiBN and TiBC coatings, *Surf. Coat. Technol.* 133-134 (2000) 131–137.
- [2] P.H. Mayrhofer, C. Mitterer, Thermal Stability of Nanostructured TiN-TiB₂ Thin Films, *Mater. Res. Soc. Symp. Proc.* 845 (2005).
- [3] C. Mitterer, P.H. Mayrhofer, M. Beschliesser, P. Losbichler, P. Warbichler, F. Hofer, P.N. Gibson, W. Gissler, H. Hruby, J. Musil, J. Vlček, Microstructure and properties of nanocomposite Ti–B–N and Ti–B–C coatings, *Surf. Coat. Technol.* 120-121 (1999) 405–411.
- [4] L. Chaleix, J. Machet, Study of the composition and of the mechanical properties of TiBN films obtained by D.C. magnetron sputtering, *Surf. Coat. Technol.* 91 (1997) 74–82.
- [5] C.X. Tian, Z.S. Wang, C.W. Zou, X.S. Tang, X. Xie, S.Q. Li, F. Liang, Z.J. Li, Y.F. Liu, F.H. Su, Ternary and quaternary TiBN and TiBCN nanocomposite coatings deposited by arc ion plating, *Surf. Coat. Technol.* 359 (2019) 445–450.
- [6] C. Mitterer, M. Rauter, P. Rödhammer, Sputter deposition of ultrahard coatings within the system Ti-B-C-N, *Surf. Coat. Technol.* 41 (1990) 351–363.
- [7] J. Wagner, D. Hochauer, C. Mitterer, M. Penoy, C. Michotte, W. Wallgram, M. Kathrein, The influence of boron content on the tribological performance of Ti–N–B coatings prepared by thermal CVD, *Surf. Coat. Technol.* 201 (2006) 4247–4252.
- [8] H. Holzschuh, Deposition of Ti–B–N (single and multilayer) and Zr–B–N coatings by chemical vapor deposition techniques on cutting tools, *Thin Solid Films* 469-470 (2004) 92–98.

- [9] M. Tkadletz, N. Schalk, C. Mitterer, J. Keckes, M. Pohler, C. Czettl, Cross-sectional characterization techniques as the basis for knowledge-based design of graded CVD TiN-TiB₂ coatings, *Int. J. Refract. Met. Hard Mater.* 71 (2018) 280–284.
- [10] I. Dreiling, C. Raisch, J. Glaser, D. Stiens, T. Chassé, Characterization and oxidation behavior of MTCVD Ti–B–N coatings, *Surf. Coat. Technol.* 206 (2011) 479–486.
- [11] I. Krajnović, W. Daves, M. Tkadletz, T. Tepperneegg, T. Klünsner, N. Schalk, C. Mitterer, C. Tritremmel, W. Ecker, C. Czettl, Finite element study of the influence of hard coatings on hard metal tool loading during milling, *Surf. Coat. Technol.* 304 (2016) 134–141.
- [12] P.H.M. Böttger, L. Braginsky, V. Shklover, E. Lewin, J. Patscheider, D.G. Cahill, M. Sobiech, Hard wear-resistant coatings with anisotropic thermal conductivity for high thermal load applications, *J. Appl. Phys.* 116 (2014) 13507.
- [13] M. Gassner, N. Schalk, M. Tkadletz, C. Czettl, C. Mitterer, Thermal crack network on CVD TiCN/ α -Al₂O₃ coated cemented carbide cutting tools, *Int. J. Refract. Met. Hard Mater.* 81 (2019) 1–6.
- [14] C. Czettl, J. Thurner, U. Schleinkofer, Knowledge based coating design of CVD TiN-TiBN-TiB₂ architecture, *Int. J. Refract. Met. Hard Mater.* 71 (2018) 330–334.
- [15] N.P. Barradas, C. Jeynes, Advanced physics and algorithms in the IBA DataFurnace, *Nucl. Instrum. Methods Phys. Res B* 266 (2008) 1875–1879.
- [16] J. Filik, A.W. Ashton, P.C.Y. Chang, P.A. Chater, S.J. Day, M. Drakopoulos, M.W. Gerring, M.L. Hart, O.V. Magdysyuk, S. Michalik, A. Smith, C.C. Tang, N.J. Terrill, M.T. Wharmby, H. Wilhelm, Processing two-dimensional X-ray diffraction and small-angle scattering data in DAWN 2, *J. Appl. Crystallogr.* 50 (2017) 959–966.

- [17] J.D. James, J.A. Spittle, S.G.R. Brown, R.W. Evans, A review of measurement techniques for the thermal expansion coefficient of metals and alloys at elevated temperatures, *Meas. Sci. Technol.* 12 (2001) R1-R15.
- [18] R.G. Munro, Material Properties of Titanium Diboride, *J. Res. Natl. Inst. Stand. Technol.* 105 (2000) 709–720.
- [19] M. Bartosik, R. Daniel, C. Mitterer, I. Matko, M. Burghammer, P.H. Mayrhofer, J. Keckes, Cross-sectional X-ray nanobeam diffraction analysis of a compositionally graded CrN_x thin film, *Thin Solid Films* 542 (2013) 1–4.
- [20] M. Stefenelli, J. Todt, A. Riedl, W. Ecker, T. Müller, R. Daniel, M. Burghammer, J. Keckes, X-ray analysis of residual stress gradients in TiN coatings by a Laplace space approach and cross-sectional nanodiffraction: a critical comparison, *J. Appl. Crystallogr.* 46 (2013) 1378–1385.
- [21] J. Almer, U. Lienert, R.L. Peng, C. Schlauer, M. Odén, Strain and texture analysis of coatings using high-energy x-rays, *J. Appl. Phys.* 94 (2003) 697–702.
- [22] M. Tkadletz, C. Hofer, C. Wüstefeld, N. Schalk, M. Motylenko, D. Rafaja, H. Holzschuh, W. Bürgin, B. Sartory, C. Mitterer, C. Czettl, Thermal stability of nanolamellar fcc-Ti_{1-x}Al_xN grown by chemical vapor deposition, *Acta Mater.* 174 (2019) 195–205.
- [23] D.G. Cahill, *Rev. Sci. Instr.* 75 (2004) 5119.
- [24] H. Nowotny, F. Benesovsky, C. Brukl, O. Schob, Die Dreistoffe: Titan-Bor-Kohlenstoff und Titan-Bor-Stickstoff, *Monatsh. Chem.* 92 403–414.
- [25] P. Scherrer, Bestimmung der Größe und der inneren Struktur von Kolloidteilchen mittels Röntgenstrahlen., *Nachrichten von der Gesellschaft der Wissenschaften zu Göttingen, Mathematisch-Physikalische Klasse* 1918 (1918) 98–100.
- [26] International Centre for Diffraction Data, PDF-2 Release, Card number 00-038-1420, 2018.

- [27] International Centre for Diffraction Data, PDF-2 Release, Card number 03-065-1073, 2018.
- [28] R. Bonetti, H.E. Hintermann, *J. Electrochem. Soc.* 124 (1977) C298.
- [29] R. Kieffer, F. Benesovsky, *Hartmetalle*, Springer Verlag, Wien, 1965, p.157.
- [30] M. Tkadletz, N. Schalk, R. Daniel, J. Keckes, C. Czettl, C. Mitterer, *Advanced characterization methods for wear resistant hard coatings: A review on recent progress*, *Surf. Coat. Technol.* 285 (2016) 31–46.
- [31] C. Saringer, C. Kicking, F. Munnik, C. Mitterer, N. Schalk, M. Tkadletz, *Thermal expansion of magnetron sputtered TiC_xN_{1-x} coatings studied by high-temperature X-ray diffraction*, *Thin Solid Films* (2019).
- [32] F. Mei, N. Shao, L. Wei, Y. Dong, G. Li, *Coherent epitaxial growth and superhardness effects of c-TiN_h-TiB₂ nanomultilayers*, *Appl. Phys. Lett.* 87 (2005) 11906.
- [33] N. Schalk, J. Keckes, C. Czettl, M. Burghammer, M. Penoy, C. Michotte, C. Mitterer, *Investigation of the origin of compressive residual stress in CVD TiB₂ hard coatings using synchrotron X-ray nanodiffraction*, *Surf. Coat. Technol.* 258 (2014) 121–126.
- [34] W. Sun, H. Xiang, F.-Z. Dai, J. Liu, Y. Zhou, *Anisotropic surface stability of TiB₂ A theoretical explanation for the easy grain coarsening*, *J. Mater. Res.* 32 (2017) 2755–2763.
- [35] M. Bartosik, R. Pitonak, J. Keckes, *In Situ High Temperature XRay Diffraction Reveals Residual Stress DepthProfiles in Blasted TiN Hard Coatings*, *Adv. Eng. Mater.* 13 (2011) 705–711.
- [36] M.W. Chase, *NIST-JANAF Thermochemical Tables: Fourth Edition*, *J. Phys. Chem. Ref. Data*, Monograph 9, 1998, pp. 1–1951.
- [37] M.K. Samani, X.Z. Ding, N. Khosravian, B. Amin-Ahmadi, Y. Yi, G. Chen, E.C. Neyts, A. Bogaerts, B.K. Tay, *Thermal conductivity of titanium nitride/titanium aluminum nitride*

multilayer coatings deposited by lateral rotating cathode arc, *Thin Solid Films* 578 (2015) 133–138.

[38] P.H. Mayrhofer, H. Clemens, C. Mitterer, Interfaces in nanostructured thin films and their influence on hardness, *Z. Metallkd.* 96 (2005) 468–480.

[39] M. Saber, C.C. Koch, R.O. Scattergood, Thermodynamic Grain Size Stabilization Models: An Overview, *Mater. Res. Lett.* 3 (2015) 65–75.

[40] E.O. Hall, The Deformation and Ageing of Mild Steel: III Discussion of Results, *Proc. Phys. Soc. Lond.* 64 (1951) 747–753.

[41] N.J. Petch, The Cleavage Strength of Polycrystals, *J. Iron Steel Inst. London.* 173 (1953) 25–28.

[42] R. Daniel, K.J. Martinschitz, J. Keckes, C. Mitterer, The origin of stresses in magnetron-sputtered thin films with zone T structures, *Acta Mater.* 58 (2010) 2621–2633.

[43] C. Kainz, N. Schalk, M. Tkadletz, C. Mitterer, C. Czettl, Microstructure and mechanical properties of CVD TiN/TiBN multilayer coatings, *Surf. Coat. Technol.*

Figures

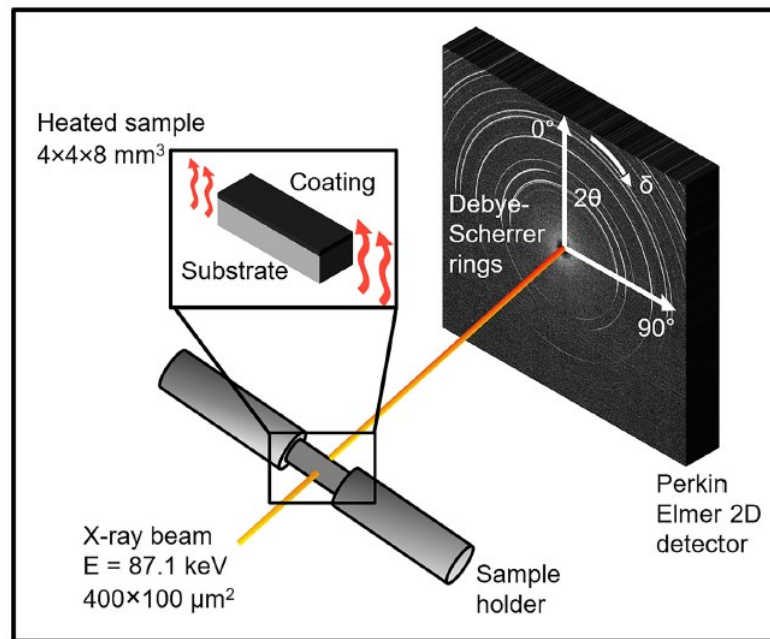


Figure 1: Schematic of the measurement set-up used to determine the temperature dependent thermal expansion and in-plane strains of the Ti(B,N) coatings. The respective sample was irradiated by a monochromatic X-ray beam perpendicular to the cross section of the sample. While the sample was heated, Debye Scherrer rings were collected in transmission geometry on a Perkin Elmer 2D detector located behind the sample.

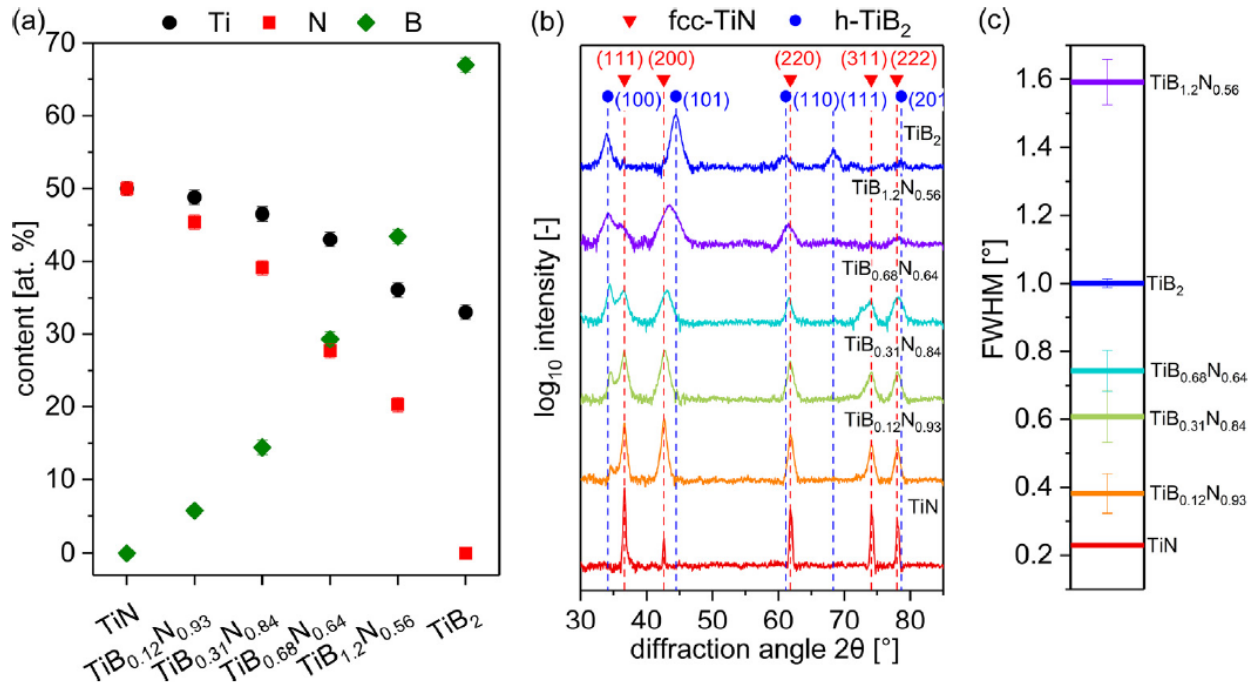


Figure 2: (a) Chemical composition, (b) X-ray diffractograms, measured in grazing incidence geometry and (c) FWHM of the Ti(B,N) coatings.

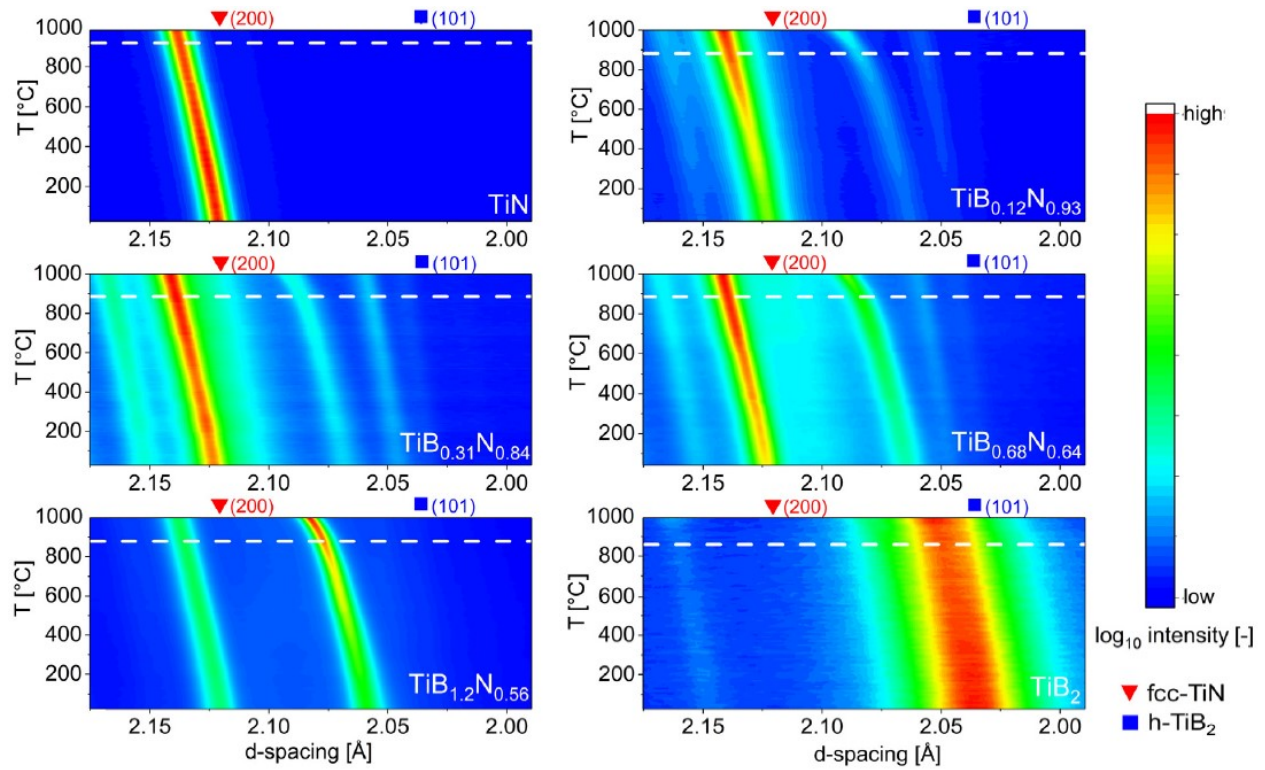


Figure 3: Phase evolution of the Ti(B,N) coatings as a function of the temperature. Literature d-spacings of the (200) reflection of fcc-TiN and the (101) reflection of h-TiB₂ are indicated by the red rectangle and blue square, respectively. The white dotted lines mark the deposition temperatures of the respective coatings.

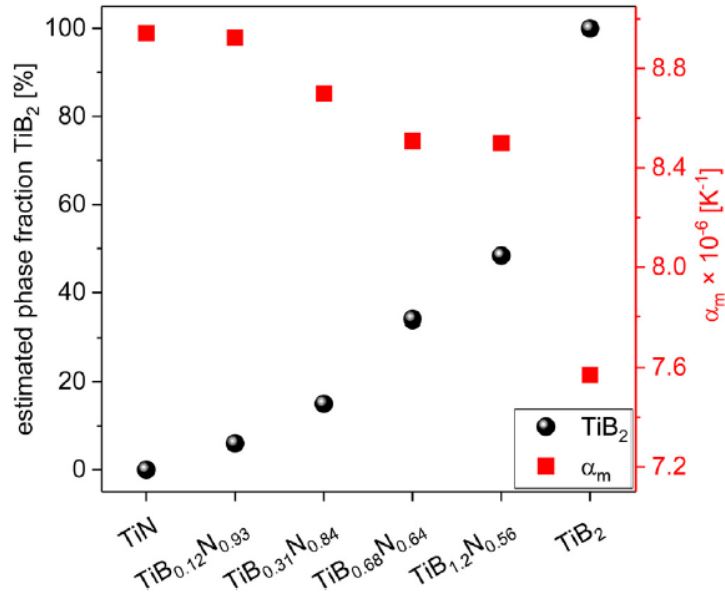


Figure 4: Estimated phase fraction of h-TiB₂ based on the available B content and mean coefficient of thermal expansion in the temperature range 25-860 °C of the Ti(B,N) coatings.

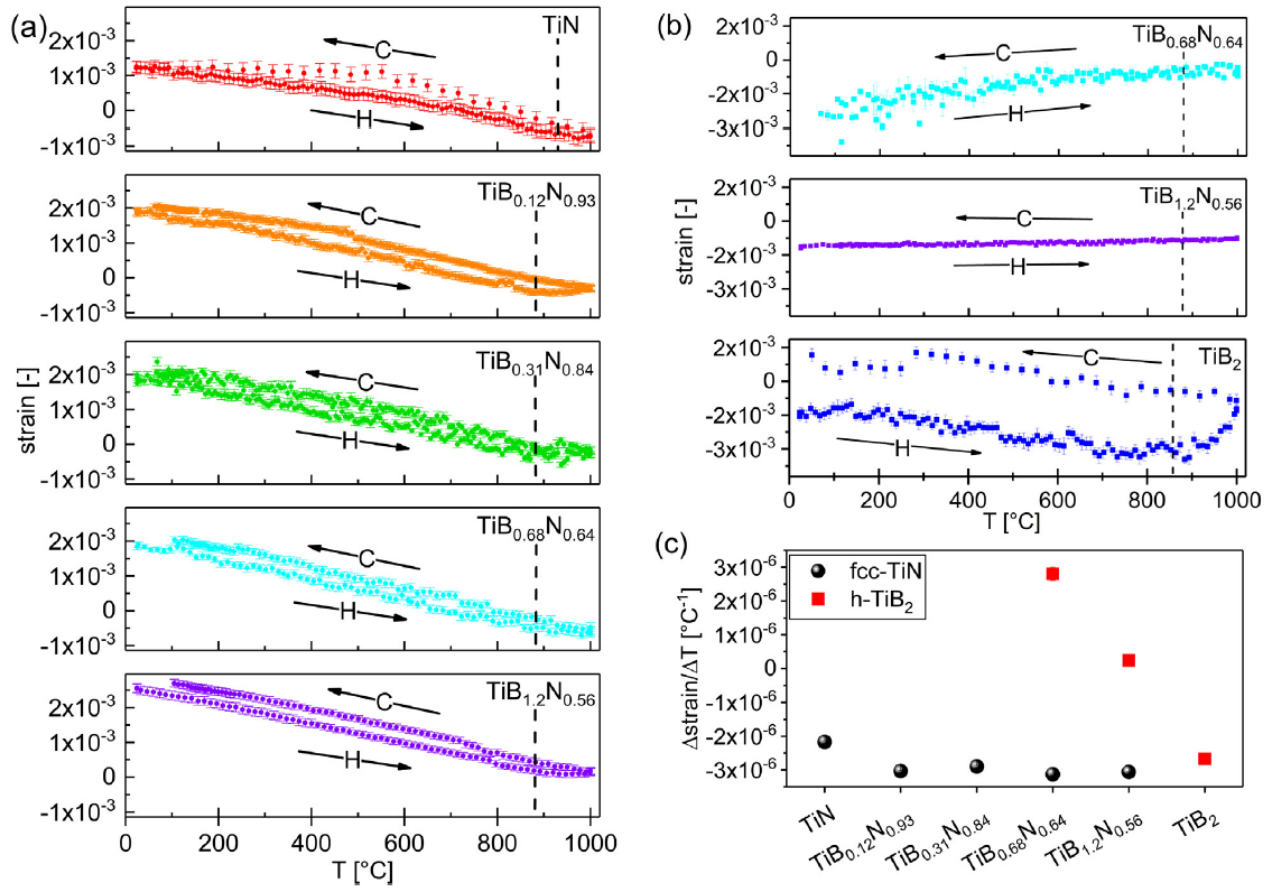


Figure 5: Evolution of the in-plane strain as a function of the temperature within the Ti(B,N) coatings. The (200) peak was evaluated in case of fcc-TiN phase (a), whereas for the h-TiB₂ phase the (101) reflection was used (b). Arrows with H depict the direction of heating, arrows with C the direction of cooling. The vertical dotted lines mark the respective deposition temperature. (c) $\Delta strain / \Delta T$ in the fcc and in the h-phase between RT and T_{dep} as a function of the B content.

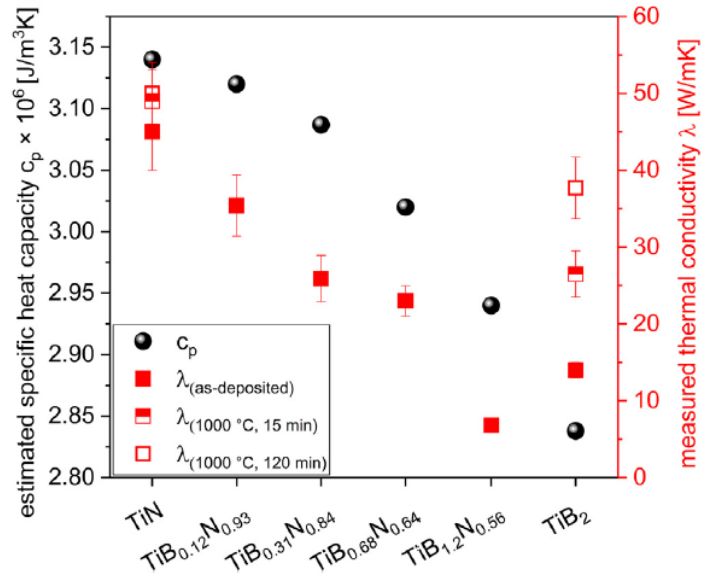


Figure 6: Estimated specific heat capacity and measured thermal conductivity of the Ti(B,N) coatings. Partly filled symbols represent measurements of coatings annealed at 1000 °C for 15 minutes, open symbols indicate annealing for 2 hours at the same temperature.

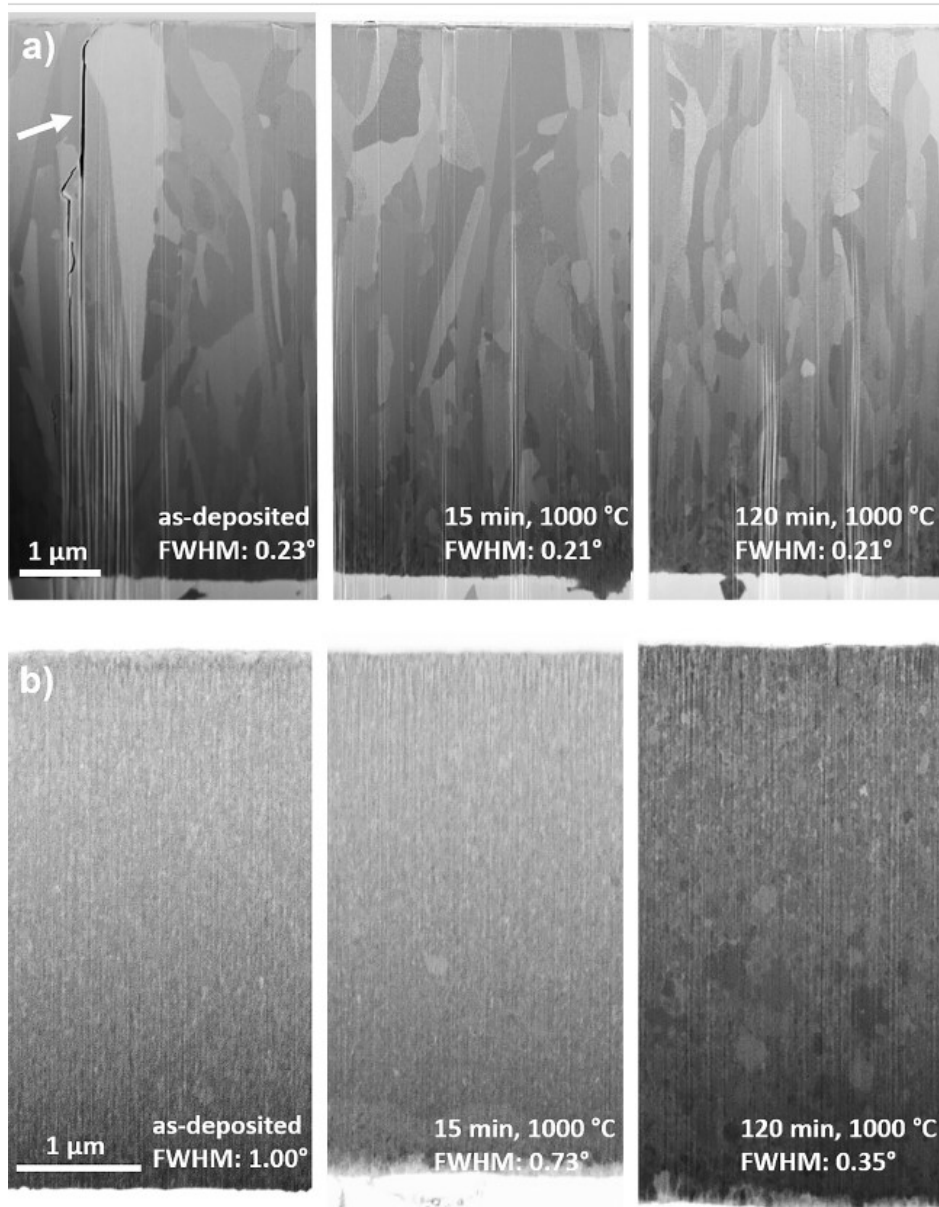


Figure 7: Cross-sectional secondary electron micrographs of a) TiN and b) TiB₂ in as-deposited state (left) and annealed at 1000 °C for 15 (middle) and 120 minutes (right) with the corresponding FWHM. A cross-sectional crack is marked by a white arrow in the as-deposited TiN (a).

Tables

Table 1: Summary of thermo-physical properties of all investigated Ti(B,N) coatings

	Coating thickness [μm]	α_m [10^{-6} K^{-1}] ¹	λ [W/mK] ²	c_p [10^6 J/ m^3K] ³
TiN	7.1	8.94	45	3.14
TiB _{0.12} N _{0.93}	5.0	8.93	35	3.12
TiB _{0.31} N _{0.84}	5.4	8.70	26	3.09
TiB _{0.68} N _{0.64}	5.9	8.51	23	3.02
TiB _{1.2} N _{0.56}	7.4	8.50	7	2.94
TiB ₂	4.1	7.57	14	2.84

¹Mean coefficient of thermal expansion (25–860 °C), ²Thermal conductivity, ³Specific heat capacity.